

LViT: Language meets Vision Transformer in Medical Image Segmentation

Zihan Li^{1,4*} Yunxiang Li² Qingde Li³ Puyang Wang⁴ You Zhang²
Dazhou Guo⁴ Le Lu⁴ Dakai Jin⁴ Qingqi Hong¹

¹ Xiamen University ² University of Texas Southwestern Medical Center
³ University of Hull ⁴ DAMO Academy, Alibaba Group

August 16, 2022

Abstract

Deep learning has been widely used in medical image segmentation and other aspects. However, the performance of existing medical image segmentation models has been limited by the challenge of obtaining sufficient number of high-quality data with the high cost of data annotation. To overcome the limitation, we propose a new vision-language medical image segmentation model LViT (Language meets Vision Transformer). In our model, medical text annotation is introduced to compensate for the quality deficiency in image data. In addition, the text information can guide the generation of pseudo labels to a certain extent and further guarantee the quality of pseudo labels in semi-supervised learning. We also propose the Exponential Pseudo label Iteration mechanism (EPI) to help extend the semi-supervised version of LViT and the Pixel-Level Attention Module (PLAM) to preserve local features of images. In our model, LV (Language-Vision) loss is designed to supervise the training of unlabeled images using text information directly. To validate the performance of LViT, we construct multimodal medical segmentation datasets (image + text) containing pathological images, X-rays, etc. Experimental results show that our proposed LViT has better segmentation performance in both fully and semi-supervised conditions. Code and datasets are available at <https://github.com/HUANGLIZI/LViT>.

1 Introduction

Medical image segmentation is one of most critical tasks in medical image analysis. In clinical practice, accurate segmentation results are often achieved manually or semi-automatically. It remains a challenging task to extract the desired object accurately, especially when the target organ to be extracted is of

*Part of the work was done when Zihan Li is an intern at DAMO Academy.

high complexity in terms of tissue structures. Recent research shows that deep learning can be a promising approach for automatic medical image segmentation, as the knowledge of experts can be learned and extracted by using a certain deep learning method. A summary of existing solutions is shown in Figure 1(a): (1) one shared encoder followed by two separate decoders [1]; (2) two separate encoders followed by one shared decode [2]; (3) two separate encoders followed by a modality interaction model [3]. However, two inherent issues concerning the creation of high quality medical image datasets severely limit the application: one is the difficulty in obtaining high-quality images, and the other one is the high cost of data annotation [4, 5]. These two issues have dramatically limited the performance improvement of medical image segmentation models. Since it is challenging to improve the quantity and quality of medical images themselves, it may be more feasible to use complementary and easy-to-access information to make up for the quality defects of medical images. Thus, we turn our attention to written medical notes accompanied with medical images. It is well known that text data of medical records are usually generated along with the patients, so no extra cost is needed to access the corresponding text data. The medical text record data and the image data are naturally complementary to each other, so the text information can compensate for the quality deficiency in the medical image data. On the other hand, expert segmentation annotation is often expensive and time-consuming, especially for new diseases like COVID-19, where high-quality annotations are even more difficult to obtain [4]. In order to address the issue of under-annotated data, some approaches have gone beyond traditional supervised learning by training their models using both labeled and more widely available unlabeled data, such as semi-supervised learning [5, 6] and weakly supervised learning [7]. However, the performance of these approaches is largely determined by the credibility of pseudo label. This is because the number of pseudo labels is much larger than ground truth labels. Therefore, the critical question to be answered is how to improve the quality of the pseudo label. To effectively address the issue, we develop a model that can be trained using the medical texts written by domain experts. By learning additional expert knowledge from text information, we can improve the quality of pseudo labels.

In summary, **the challenges exist in two aspects**: **1)** How to improve the segmentation performance by using the existing image-text information; **2)** How to make full use of text information to guarantee the quality of pseudo labels. To address **the first challenge**, We propose the LViT model (Figure 1(b)), which is innovative in processing images and text. In LViT, the text feature vector is obtained by using the Embedding layer instead of Text Encoder, which can further reduce the number of parameters in the model. In addition, a hybrid CNN-Transformer structure is able to better merge text information and encode global features with Transformer while retaining the CNN's ability to extract local features from images. To address **the second challenge**, we design an exponential pseudo label iteration mechanism (EPI) for the proposed LViT, aiming to cross-utilize the label information of labeled data and the latent information of unlabeled data. The EPI indirectly introduces text information

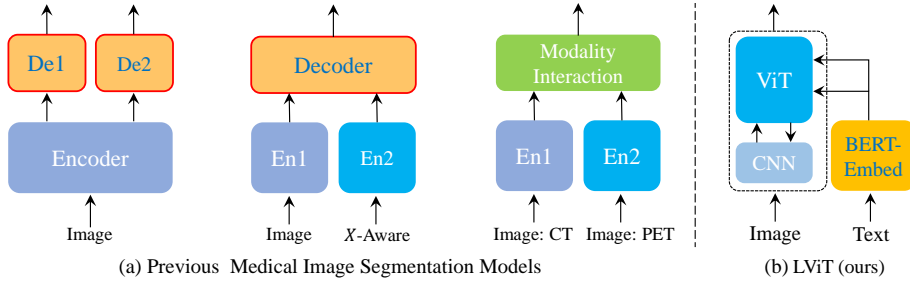


Figure 1: Comparison of current medical image segmentation models and our proposed LViT model.

to refine the pseudo label progressively using the Exponential Moving Average (EMA)[8]. In addition, the LV (Language-Vision) loss is designed to directly utilize text to supervise the training of unlabeled medical images. To validate the performance of LViT, we construct multimodal medical image segmentation datasets containing pathological images (MoNuSeg [9]) and X-rays (QaTa-COV19 [10]). Results show that LViT has superior segmentation performance, achieving 81.01% Dice score and 68.2% mIoU on the MoNuSeg dataset and 83.66% Dice score and 75.11% mIoU on the QaTa-COV19 dataset. And it is worth noting that LViT using 1/4 of the train set label can still have the same performance as the fully supervised segmentation method.

2 Related work

Semantic segmentation can be considered as the work for pixel-level image classification, and thus many image classification networks have been extended [11, 12] to implement semantic segmentation, with FCN [11] being commonly considered as the first semantic segmentation network for pixel-wise prediction. Among them, U-Net [13] is considered as a pioneer in medical image segmentation. Based on this, UNet++ [14] improved the skip connection of U-Net. However, most of the above methods are very sensitive to the quantity and quality of the data, resulting in limited generalization performance of the models. Therefore, some approaches [5, 15, 16] have explored the application of semi-supervised learning to medical image segmentation. The problem of lacking data and its annotation can also be further mitigated by introducing multiple modalities into the learning models. Inspired by this, Radford et al. proposed CLIP [17], which uses contrast learning to learn image representations on a dataset of 400 million pairs (image, text) from scratch. And in the natural image semantic segmentation, there are studies [18, 19, 20] that have begun to use text information to improve the segmentation capabilities of models. In the field of medical image analysis, there are some related works too[21, 22]. However, unlike existing multimodal solutions [17, 21, 22], LViT don't use text encoder and contrastive learning on explicitly aligned images and text. We only use text embedding without additional encoder to reach state-of-the-art (SOTA) performance. And the rationality of our approach will be proved in Section 4.4.

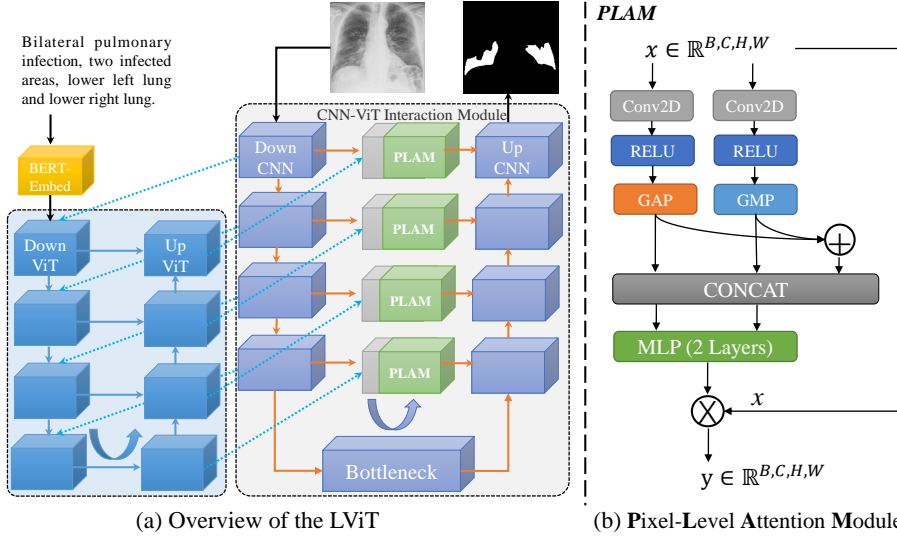


Figure 2: Illustration of (a) the proposed LViT model, and (b) PLAM. The proposed LViT model is a Double-U structure formed by combining a U-shape CNN branch with a U-shaped ViT branch.

3 Method

As shown in Figure 2, the proposed LViT model is a Double-U structure consisting of a U-shaped CNN branch and a U-shaped Transformer branch. The CNN branch acts as the source of information input and the segmentation head of prediction output, and the ViT branch is used to merge image and text information, where we exploit the ability of Transformer to process cross-modality information. After a simple vectorization of the text, the text vector is merged with the image vector and send to the U-shaped ViT branch for processing. Then, we pass the fusion information of the corresponding size back to the U-shape CNN branch at each layer for the final segmentation prediction output. In addition, a pixel-level attention module (PLAM) is set at the skip connection position of the U-shape CNN branch. With PLAM, LViT is able to retain as much local feature information of the image as possible. We also conduct ablation experiments to demonstrate the effectiveness of each module.

3.1 LViT Model

U-shape CNN Branch. As shown in Figure 2(a), the U-shaped CNN branch is used to receive the image information and act as segmentation head to output the prediction mask. The Conv, BatchNorm(BN), and ReLU activation layers are utilized to compose each CNN module. And image feature are downsampled between each DownCNN module using the MaxPool layer. Concatenate operation is performed between each UpCNN module. The specific process of each CNN

module is shown in Eqn. 1 and 2,

$$\text{DownCNN}_i = \text{Relu}(\text{BN}_i(\text{Conv}_i)) \quad (1)$$

$$Y_{\text{DownCNN},i+1} = \text{MaxPool}(\text{DownCNN}_i(Y_{\text{DownCNN},i})) \quad (2)$$

where $Y_{\text{DownCNN},i}$ represents the input of the i -th DownCNN module, which becomes $Y_{\text{DownCNN},i+1}$ after the downsampling of the i -th DownCNN module and the MaxPool layer. In addition, we design the CNN-ViT interaction module using methods such as upsampling to align the features from ViT, as the details of CNN-ViT interaction module are shown in the appendix. The reconstructed ViT features are also connected with CNN feature by residuals to form CNN-ViT interaction features. In addition, to further improve the segmentation capability for local features, PLAM is designed at the skip connection in the U-shaped CNN branch. So the CNN-ViT interaction features will be fed into PLAM, then transferred to the UpCNN module to give the upward information layer by layer.

U-shape ViT Branch. Referring to the U-shaped CNN branch, the U-shaped ViT branch is designed for merging image features and text features. As shown in Figure 2(a), the first layer DownViT module receives the text feature input from BERT-Embed [23] and the image feature input from the first layer DownCNN module. The pretraining model of the BERT-Embed is the BERT_12_768_12 model, which can convert a single word into a 768-dimensional word vector. The specific cross-modal feature merging operation is expressed by the following equations,

$$Y_{\text{DownViT},1} = \text{ViT}(x_{\text{img},1} + \text{CTBN}(x_{\text{text}})) \quad (3)$$

$$x_{\text{img},i} = \text{PatchEmbedding}(Y_{\text{DownCNN},i}) \quad (4)$$

$$x' = \text{ViT}_1(x) = \text{MHSA}(\text{LN}(x)) + x \quad (5)$$

$$Y = \text{ViT}_2(x') = \text{MLP}(\text{LN}(x')) + x' \quad (6)$$

where $x_{\text{img},i}$ represents the image features from DownCNN, x_{text} represents the text features, and PatchEmbedding can help $Y_{\text{DownCNN},i}$ form the embedding features $x_{\text{img},i}$. ViT represents the Transformer encoder[24], i.e., $Y = \text{ViT}(x) = \text{ViT}_2(\text{ViT}_1(x))$. ViT consists of the Multi-headed Self-attention (MHSA) module and the MLP layer. And LN represents the normalization layer. The CTBN block also consists of the Conv layer, BatchNorm layer, and ReLU activation layer for aligning the feature dimensions of $x_{\text{img},1}$ and x_{text} . The subsequent DownViT modules of layers 2, 3, and 4 receive both feature from the upper DownViT module and the feature from the DownCNN module of the corresponding layer, as shown in Eqn. 7,

$$Y_{\text{DownViT},i+1} = \text{ViT}(Y_{\text{DownViT},i} + x_{\text{img},i+1}) \quad (7)$$

where $i=1,2,3$. The features of the corresponding size are then transferred back to the CNN-ViT interaction module through the UpViT module. And the feature is merged with the feature from the DownCNN module of the corresponding layer. This will maximize the extraction of image global features and avoid the oscillation of the model performance due to the inaccuracy of text annotation.

Pixel-Level Attention Module (PLAM). As shown in Figure 2(b), PLAM is designed to preserve the local features of the image and further merge the semantic features in text. Referring to convolutional block attention module (CBAM)[25], PLAM uses parallel branches for Global Average Pooling (GAP) and Global Max Pooling (GMP). We also incorporate the concat and add operations. The add operation will help merge the corresponding channel features with similar semantics and save computation. In contrast, the concat operation can integrate the feature information more intuitively and help preserve the original features of each part. After concat the feature information, we use the MLP structure and the multiplication operation to help align the feature size, as shown in Eqn. 8,

$$Y = \text{MLP}(x_{\text{cat}}) \otimes x. \quad (8)$$

3.2 Exponential Pseudo-label Iteration mechanism (EPI)

In this section, we present proposed **E**xponential **P**seudo label **I**teration mechanism (EPI), which is designed to help extend the semi-supervised version of LViT. In EPI, the pseudo label is iteratively updated using the idea of EMA [8], as shown in Figure 3(a) and Eqn. 9,

$$P_t = \beta \cdot P_{t-1} + (1 - \beta) \cdot P_t \quad (9)$$

where P_{t-1} represents the prediction of model M_{t-1} , and β is set as the momentum parameter to 0.99. It is worth noting that here P_{t-1} is an N -dimensional prediction vector, where N represents the number of category classes, and each dimension represents the prediction probability. Therefore, EPI can gradually optimize the segmentation prediction results of the model for each unlabeled pixel and be robustness to noisy label. This is because we do not simply use the pseudo label predicted by one generation of model as the target for the next-generation model, which can avoid sharp deterioration of the pseudo label quality. The theoretical proof for the effectiveness of EPI algorithm is as follows.

Proof: The basic assumption for the EPI algorithm is the model weights will dither around the actual optimum in the last n generations, and therefore the pseudo label predicted by the model will also dither around the actual mask in the last n generations. We expand P_t around t in Eqn. 9 to Eqn.10,

$$P_t = \beta^n \cdot P_{t-n} + (1 - \beta) \cdot (\beta^{n-1} P_{t-n+1} + \cdots + \beta^0 P_t). \quad (10)$$

In particular, we let $n = 1/(1 - \beta)$ and $\beta^n = \beta^{\frac{1}{1-\beta}} \approx \frac{1}{e}$. So for the first $1/(1 - \beta)$ generations, P_t decays to a weighted average of $1/e$. Further, we introduce an adjustment gradient g_{t-1} for the predicted label P_{t-1} , which leads to Eqn. 11,

$$P_t = P_{t-1} - g_{t-1} = P_{t-2} - g_{t-1} - g_{t-2} = \cdots = P_1 - \sum_{i=1}^{n-1} g_i. \quad (11)$$

Similarly, we extend Eqn. 10 to Eqn. 12 when $t = n$ and $P_0 \approx P_1$,

$$\begin{aligned}
P_t &= \beta^n \cdot P_0 + (1 - \beta) \cdot (\beta^{n-1} P_1 + \beta^{n-2} P_2 + \cdots + \beta^0 P_n) \\
&= \beta^n \cdot P_0 + (1 - \beta) \cdot \left(\beta^{n-1} P_1 + \beta^{n-2} (P_1 - g_1) + \cdots + \beta^0 \left(P_1 - \sum_{i=1}^{n-1} g_i \right) \right) \\
&= \beta^n \cdot P_0 + (1 - \beta) \cdot \left(\frac{1 - \beta^n}{1 - \beta} P_1 - \sum_{i=1}^{n-1} \frac{(1 - \beta^{n-i}) g_i}{1 - \beta} \right) \\
&= \beta^n \cdot P_0 + (1 - \beta^n) \cdot P_1 - \sum_{i=1}^{n-1} (1 - \beta^{n-i}) g_i \approx P_1 - \sum_{i=1}^{n-1} (1 - \beta^{n-i}) g_i.
\end{aligned} \tag{12}$$

Comparing with Eqn.11, it can be seen from Eqn.12 that the EPI algorithm adds the weight coefficient $1 - \beta^{n-i}$ for the gradient descent step of the i -th iteration. $1 - \beta^{n-i}$ will decreases as i increases, so the change of pseudo label is finally stabilized and obtain the pseudo label with high confidence.

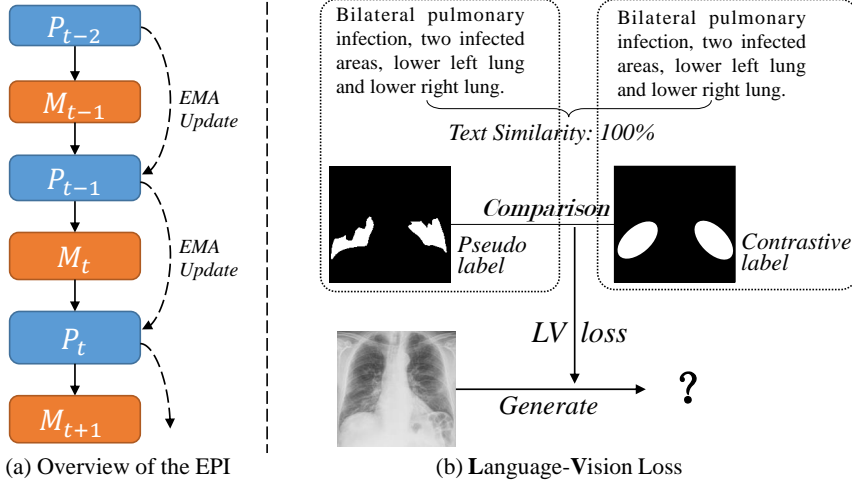


Figure 3: Illustration of (a) Exponential Pseudo-label Iteration mechanism (EPI), and (b) LV Loss.

3.3 LV (Language-Vision) Loss

To further utilize the text information to guide the pseudo-label generation, we design the LV (Language-Vision) loss function, as shown in Figure 3(b). Taking the QaTa-COV19 dataset as an example, we can use different structured text information to form the corresponding mask (the contrastive label in Figure 3(b)). For the MoNuSeg dataset, we directly use the mask in labeled training set as the contrastive label. And the cosine similarity between the texts is shown in Eqn. 13,

$$\text{TextSim} = \frac{x_{\text{text},p} \cdot x_{\text{text},c}}{|x_{\text{text},p}| \times |x_{\text{text},c}|} \tag{13}$$

where $x_{text,p}$ represents the text feature vector corresponding to the pseudo label, and $x_{text,c}$ represents the text feature vector corresponding to the contrastive label. According to *TextSim*, we select the contrastive text with the highest similarity and calculate the cosine similarity between the segmentation mask to form L_{LV} corresponding to that text, as shown in Eqn. 14 and 15,

$$\text{ImgSim} = \frac{x_{img,p} \cdot x_{img,c}}{|x_{img,p}| \times |x_{img,c}|} \quad (14)$$

$$L_{LV} = 1 - \text{ImgSim} \quad (15)$$

4 Experiments

4.1 Setup

Two datasets are used in the experiments to evaluate the performance. One is the MoNuSeg dataset [9] obtained from the MICCAI 2018 MoNuSeg Challenge. The training set consists of 30 images with 21,623 single kernel annotations. The other is the QaTa-COV19 dataset [10], which is compiled by researchers from Qatar University and Tampere University. The dataset consists of 9258 COVID-19 chest radiographs with manual annotations of COVID-19 lesions for the first time. In addition, text annotations for the datasets are extended by us to be used for training the vision-language model. The loss function we use is shown in Eqn. 16, where L_{Dice} means dice loss and L_{CE} means cross-entropy loss. For the unlabeled data, an additional term on the loss L_{LV} is introduced with $\alpha = 0.1$ as shown in Eqn. 17. Dice and mIoU are used to evaluate the segmentation performance. And early stop mechanism is used during training phase. More implementation details can be found in the appendix.

$$L_{sup} = (L_{Dice} + L_{CE})/2 \quad (16)$$

$$L_{unsup} = (L_{Dice} + L_{CE})/2 + \alpha \cdot L_{LV} \quad (17)$$

4.2 Comparison with State-of-the-Art (SOTA) Methods

We compare the performance of our LViT model with several CNN and Transformer based segmentation models. The number of network parameters and the computational cost of different methods are also reported. Note that the numbers after the methods refer to the ratio of labels used, e.g., LViT-T (1/2) refers to the experimental results of the LViT-T model using 1/2 of the train set labels. And LViT-T means the **Tiny** version of LViT. The quantitative experimental results are listed in Table 1.

Experimental results on the QaTa-COV19 dataset show that LViT-TW/LViT-T is able to achieve better performance than the previous SOTA method with a smaller number of parameters and a lower computational cost. For example, LViT-T improves the Dice score by 3.24% and the mIoU by 4.3% compared to the suboptimal nnUNet. It is also worth noting that LViT-T still outperforms other SOTA methods even when only 1/4 of the training labels are

Table 1: Performance comparison between our method (LViT) and other state-of-the-art methods on QaTa-COV19 and MoNuSeg datasets. The "W" in LViT-TW refers to without the text information.

| Method | Param (M) | Flops (G) | QaTa-COV19 | | MoNuSeg | |
|-----------------|---------------|---------------|--------------|--------------|--------------|--------------|
| | | | Dice (%) | mIoU (%) | Dice (%) | mIoU (%) |
| U-Net [13] | 14.8 | 50.3 | 79.02 | 69.46 | 76.45 | 62.86 |
| UNet++ [14] | 74.5 | 94.6 | 79.62 | 70.25 | 77.01 | 63.04 |
| AttUNet [26] | 34.9 | 101.9 | 79.31 | 70.04 | 76.67 | 63.47 |
| nnUNet [27] | 19.1 | 412.7 | 80.42 | 70.81 | 80.06 | 66.87 |
| MedT [28] | 98.3 | 131.5 | 77.47 | 67.51 | 77.46 | 63.37 |
| TransUNet [29] | 105 | 56.7 | 78.63 | 69.13 | 78.53 | 65.05 |
| GTUNet [20] | 24.8 | 42.6 | 79.17 | 69.65 | 79.26 | 65.94 |
| Swin-UNet [30] | 82.3 | 67.3 | 78.07 | 68.34 | 77.69 | 63.77 |
| UCTransNet [31] | 65.6 | 63.2 | 79.15 | 69.60 | 79.87 | 66.68 |
| LViT-TW(1/4) | | | 79.08 | 69.42 | 79.94 | 66.80 |
| LViT-T (1/4) | | | 80.95 | 71.31 | 80.09 | 66.97 |
| LViT-TW(1/2) | LViT-TW: 28.0 | LViT-TW: 54.0 | 80.35 | 70.74 | 80.11 | 67.04 |
| LViT-T (1/2) | LViT-T: 29.7 | LViT-T: 54.1 | 82.73 | 73.99 | 80.25 | 67.17 |
| LViT-TW | | | 81.12 | 71.37 | 80.33 | 67.24 |
| LViT-T | | | 83.66 | 75.11 | 80.36 | 67.31 |

used. Similarly, it can be seen that LViT-T has a 2.54% higher Dice score and a 4.05% better mIoU score than LViT-TW. This also indicates that introducing text information is able to improve model performance effectively. A similar trend is observed for the MoNuSeg dataset. On the MoNuSeg dataset, compared to UCTransNet, LViT-T improves the Dice value by 0.49% and the mIoU value by 0.63%. Even LViT-TW and LViT-T (1/4) can achieve comparable performance to nnUNet and UCTransNet.

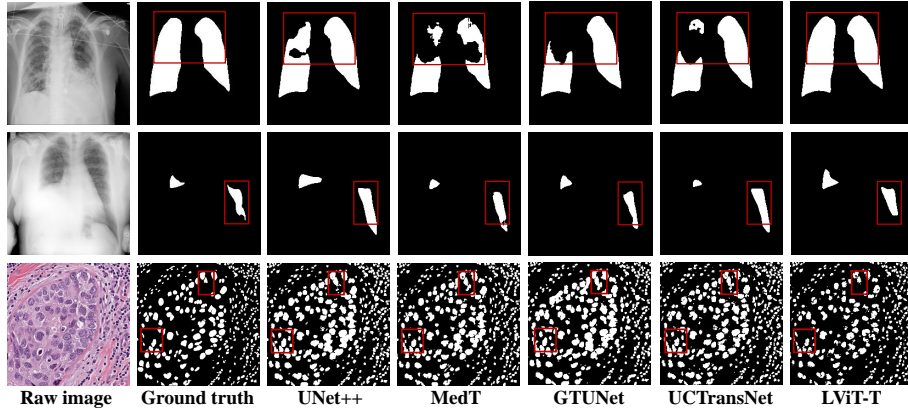


Figure 4: Qualitative results on QaTa-COV19 and MoNuSeg datasets.

The qualitative results of our model and other state-of-the-art methods on MoNuSeg and QaTa-COV19 datasets are shown in Figure 4, where four baseline methods are selected for comparison. Qualitative results shows that LViT-T has excellent semantic segmentation capabilities, especially when compared to other SOTA methods where the mis-segmentation phenomenon is greatly reduced.

As can be seen from the red boxes in Figure 4, UNet++, MedT, GTUNet and TransUNet all have more severe mis-segmentation than LViT. It also shows the introduction of text information in our learning mechanism can better guide the training of the model, and consequently lead to more accurate segmentation.

4.3 Ablation Study

A series of ablation experiments are used to verify the performance of the LViT model. The performance of the LViT model is explored in three aspects, including the comparison of proposed components, model size and hyper-parameters.

The Effectiveness of Proposed Components. Relevant ablation experiments are conducted for our proposed method, and the relevant experimental results are shown in Table 2. We explore the effectiveness of the improvements from four perspectives, including DownViT, UpViT, PLAM, and Text. The Text refers to the text information. All of them are effective based on experimental results, where the performance improvement brought by Text is the most obvious. Relevant ablation experiments are also performed to address our innovative points in semi-supervision. We explore the effectiveness of the improvement from three perspectives, including EPI, Text, and L_{LV} . From the experimental results, it can be seen that the improvements of EPI, Text, and L_{LV} are effective. Among them, by introducing text annotation information, the Dice score improves by 1.59%, and mIoU improves by 1.66% compared to LViT with only 1/4 of the train set label supervision. And by introducing EPI mechanism, the semi-supervised performance of LViT is guaranteed to be comparable to the fully supervised performance of U-Net. Finally, the continuous improvement of model performance is also ensured by introducing L_{LV} .

Table 2: Ablation study on effectiveness of supervised components: DownViT, UpViT, PLAM, Text & semi-supervised components: EPI, Text, Loss L_{LV} on QaTa-COV19 dataset.

| Method | CNN | DownViT | UpViT | PLAM | Text | EPI | L_{LV} | Dice (%) | mIoU (%) |
|--------------|-----|---------|-------|------|------|-----|----------|--------------|--------------|
| U-Net | ✓ | | | | | | | 79.02 | 69.46 |
| LViT-T | ✓ | ✓ | | | | | | 80.73 | 70.96 |
| | ✓ | ✓ | ✓ | | | | | 80.85 | 71.12 |
| | ✓ | ✓ | ✓ | ✓ | | | | 81.12 | 71.37 |
| | ✓ | ✓ | ✓ | ✓ | ✓ | | | 80.52 | 70.43 |
| | ✓ | ✓ | ✓ | ✓ | ✓ | ✓ | | 83.66 | 75.11 |
| LViT-T (1/4) | ✓ | ✓ | ✓ | ✓ | ✓ | ✓ | | 79.08 | 69.42 |
| | ✓ | ✓ | ✓ | ✓ | ✓ | ✓ | | 80.67 | 71.08 |
| | ✓ | ✓ | ✓ | ✓ | ✓ | ✓ | ✓ | 80.95 | 71.31 |

Ablation Study on Model Size. We conduct ablation experiments for model sizes to investigate the specific performance of LViT with different model sizes. The experiments are conducted on two datasets, QaTa-COV19 and MoNuSeg, with eight different model sizes, namely, LViT-TW/LViT-T, LViT-SW/LViT-S, LViT-MW/LViT-M, LViT-LW/LViT-L, where "W" refers to with-

out the text information. And the differences between different versions of LViT are in the number of Transformer layers in the DownViT module and UpViT module, where LViT-TW/LViT-T has only 1 Transformer layer per ViT module, and LViT-SW/LViT-S has 4 Transformer layers per ViT module. LViT-MW/LViT-M has 6 Transformer layers per ViT module, and LViT-LW/LViT-L has 12 Transformer layers per ViT module. The experimental results are shown in Table 3.

Table 3: Ablation study on different Model Size: LViT-T, LViT-S, LViT-M, LViT-L.

| Model Size | Param(M) | Flops(G) | QaTa-COV19 | | MoNuSeg | |
|------------|------------------|------------------|--------------|--------------|--------------|--------------|
| | | | Dice (%) | mIoU (%) | Dice (%) | mIoU (%) |
| LViT-TW | | | 81.12 | 71.37 | 80.33 | 67.24 |
| LViT-T | LViT-TW: 28.0 | LViT-TW: 54.0 | 83.66 | 75.11 | 80.36 | 67.31 |
| LViT-SW | LViT-SW: 53.1 | LViT-SW: 63.8 | 81.54 | 71.91 | 80.27 | 67.20 |
| LViT-S | LViT-MW: 69.8 | LViT-MW: 70.4 | 83.41 | 74.84 | 80.50 | 67.36 |
| LViT-MW | LViT-LW: 120.1 | LViT-LW: 90.1 | 81.59 | 71.82 | 80.38 | 67.33 |
| LViT-M | | | 83.63 | 75.28 | 80.39 | 67.37 |
| LViT-LW | LViT: LViT-W+1.7 | LViT: LViT-W+0.1 | 81.40 | 71.43 | 80.66 | 67.71 |
| LViT-L | | | 82.74 | 73.00 | 81.01 | 68.20 |

According to the experimental results, the increases of model size does not lead to the performance improvement on the QaTa-COV19 dataset. Besides, the model performance is further limited when model size increasing to LViT-LW. This could be due to the fact that the increase of the number of parameters will lead to the increase of the probability of model overfitting, so the performance of LViT-LW/LViT-L may no longer be as good as it should be. In contrast, the positive correlation between model performance and model size is followed on the MoNuSeg dataset. Besides, it is worth noting that LViT has only 1.7M more parameters and 0.1G more computation than LViT-W, which indicates the number of parameters and the amount of computation brought by the text information is far more valuable than the size change of the model itself.

4.4 Interpretability Study

The interpretability study is performed on the QaTa-COV19 dataset to explore whether the LViT network can notice lesion regions and whether the introduction of text information enhances the attention to lesion regions. We use GradCAM [32] to compare the activation for regions of attention. Figure 5 shows that UNet++, MedT, GTUNet and UCTransNet all have different degrees of mis-activation regions. For example, the case of total lung infection only activates half of the lung region in other methods. In contrast, by introducing text information in our model, more regions can be activated, and the edge profile of the activated regions of interest is more consistent with the ground truth. Therefore, the localization of lesion regions can be learned by introducing text embedding. In addition, we conduct more experiments to explore how the introduction of text information specifically helps activate regions, as shown in Figure 6. We perform

activation mapping in DownCNN1, DownCNN2, DownCNN3, DownCNN4, and DownViT1, respectively, where DownCNN1 and DownViT1 represent the first layer DownCNN and the first layer DownViT, respectively, where the text information is input to the model through DownViT1, so the difference in activation regions between DownViT1 and DownCNN1 can be approximated as brought by the text information. And the CAM output of LViT-TW and LViT-T shows the final activation difference caused by the text information. It can be seen that the activation effect of the region of interest of DownViT1 is similar to that of DownCNN4. It is also worth noting that image feature of DownViT1 comes from DownCNN1, which failed to activate the lesion region but only activated the lung boundary. However, DownViT1 can directly activate the relevant lesion region by introducing text information. And it indicates that the text information can effectively help locate lesion region in the lung, thus prompting the network to focus more on the region referred to by the text information. By comparing the regions of interest for LViT-TW/LViT-T, we find text information can help reduce the probability of mis-segmentation.

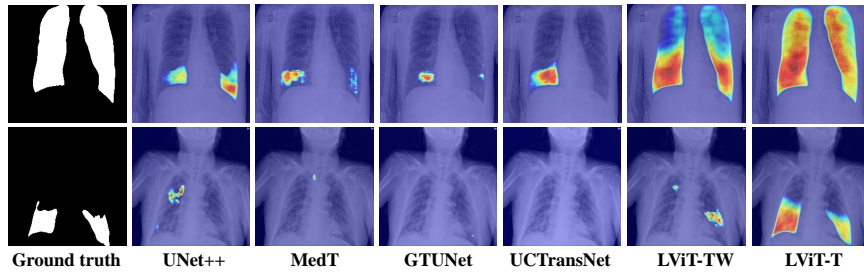


Figure 5: Saliency map for interpretability study of different approaches on QaTa-COV19 dataset.

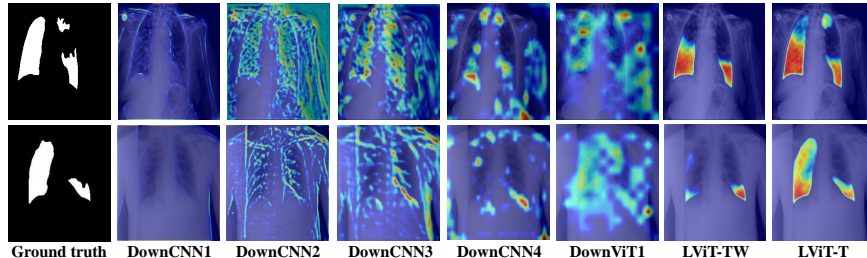


Figure 6: Saliency map for interpretability study of different layers of LViT on QaTa-COV19 dataset.

5 Conclusion

In this paper, we propose a new vision-language medical image segmentation model LViT, which leverages medical text annotation to compensate for the quality deficiency in image data and guide the generation of pseudo labels in semi-supervised learning. Multimodal medical segmentation datasets (image + text)

are constructed to evaluate the performance of LViT, and experimental results show that our model has better segmentation performance in both fully and semi-supervised conditions. Currently, the proposed model is only experimented on 2D medical data. In our future work, we will extend our model to conduct experiments on 3D medical data to verify its generality.

References

- [1] Sihong Chen, Kai Ma, and Yefeng Zheng. Med3d: Transfer learning for 3d medical image analysis. *arXiv preprint arXiv:1904.00625*, 2019.
- [2] Jiacheng Wang, Lan Wei, Liansheng Wang, Qichao Zhou, Lei Zhu, and Jing Qin. Boundary-aware transformers for skin lesion segmentation. In *International Conference on Medical Image Computing and Computer-Assisted Intervention*, pages 206–216. Springer, 2021.
- [3] Zhuotun Zhu, Dakai Jin, Ke Yan, Tsung-Ying Ho, Xianghua Ye, Dazhou Guo, Chun-Hung Chao, Jing Xiao, Alan Yuille, and Le Lu. Lymph node gross tumor volume detection and segmentation via distance-based gating using 3d ct/pet imaging in radiotherapy. In *International Conference on Medical Image Computing and Computer-Assisted Intervention*, pages 753–762. Springer, 2020.
- [4] Xiaoman Zhang, Weidi Xie, Chaoqin Huang, Ya Zhang, and Yanfeng Wang. Self-supervised tumor segmentation through layer decomposition. *arXiv preprint arXiv:2109.03230*, 2021.
- [5] Yanwen Li, Luyang Luo, Huangjing Lin, Hao Chen, and Pheng-Ann Heng. Dual-consistency semi-supervised learning with uncertainty quantification for covid-19 lesion segmentation from ct images. In *International Conference on Medical Image Computing and Computer-Assisted Intervention*, pages 199–209. Springer, 2021.
- [6] Lequan Yu, Shujun Wang, Xiaomeng Li, Chi-Wing Fu, and Pheng-Ann Heng. Uncertainty-aware self-ensembling model for semi-supervised 3d left atrium segmentation. In *International Conference on Medical Image Computing and Computer-Assisted Intervention*, pages 605–613. Springer, 2019.
- [7] Xinyang Feng, Jie Yang, Andrew F Laine, and Elsa D Angelini. Discriminative localization in cnns for weakly-supervised segmentation of pulmonary nodules. In *International conference on medical image computing and computer-assisted intervention*, pages 568–576. Springer, 2017.
- [8] Jean-Bastien Grill, Florian Strub, Florent Altché, Corentin Tallec, Pierre Richemond, Elena Buchatskaya, Carl Doersch, Bernardo Avila Pires, Zhaohan Guo, Mohammad Gheshlaghi Azar, et al. Bootstrap your own latent-a

new approach to self-supervised learning. *Advances in Neural Information Processing Systems*, 33:21271–21284, 2020.

- [9] Neeraj Kumar, Ruchika Verma, Deepak Anand, Yanning Zhou, Omer Fahri Onder, Efstratios Tsougenis, Hao Chen, Pheng-Ann Heng, Jiahui Li, Zhiqiang Hu, et al. A multi-organ nucleus segmentation challenge. *IEEE transactions on medical imaging*, 39(5):1380–1391, 2019.
- [10] Aysen Degerli, Serkan Kiranyaz, Muhammad EH Chowdhury, and Moncef Gabbouj. Osegnet: Operational segmentation network for covid-19 detection using chest x-ray images. *arXiv preprint arXiv:2202.10185*, 2022.
- [11] Jonathan Long, Evan Shelhamer, and Trevor Darrell. Fully convolutional networks for semantic segmentation. In *Proceedings of the IEEE conference on computer vision and pattern recognition*, pages 3431–3440, 2015.
- [12] Liang-Chieh Chen, George Papandreou, Iasonas Kokkinos, Kevin Murphy, and Alan L Yuille. Deeplab: Semantic image segmentation with deep convolutional nets, atrous convolution, and fully connected crfs. *IEEE transactions on pattern analysis and machine intelligence*, 40(4):834–848, 2017.
- [13] Olaf Ronneberger, Philipp Fischer, and Thomas Brox. U-net: Convolutional networks for biomedical image segmentation. In *International Conference on Medical image computing and computer-assisted intervention*, pages 234–241. Springer, 2015.
- [14] Zongwei Zhou, Md Mahfuzur Rahman Siddiquee, Nima Tajbakhsh, and Jianming Liang. Unet++: A nested u-net architecture for medical image segmentation. In *Deep learning in medical image analysis and multimodal learning for clinical decision support*, pages 3–11. Springer, 2018.
- [15] Yingda Xia, Dong Yang, Zhiding Yu, Fengze Liu, Jinzheng Cai, Lequan Yu, Zhuotun Zhu, Daguang Xu, Alan Yuille, and Holger Roth. Uncertainty-aware multi-view co-training for semi-supervised medical image segmentation and domain adaptation. *Medical Image Analysis*, 65:101766, 2020.
- [16] Quande Liu, Lequan Yu, Luyang Luo, Qi Dou, and Pheng Ann Heng. Semi-supervised medical image classification with relation-driven self-ensembling model. *IEEE transactions on medical imaging*, 39(11):3429–3440, 2020.
- [17] Alec Radford, Jong Wook Kim, Chris Hallacy, Aditya Ramesh, Gabriel Goh, Sandhini Agarwal, Girish Sastry, Amanda Askell, Pamela Mishkin, Jack Clark, et al. Learning transferable visual models from natural language supervision. In *International Conference on Machine Learning*, pages 8748–8763. PMLR, 2021.
- [18] Wei Yin, Yifan Liu, Chunhua Shen, Anton van den Hengel, and Baichuan Sun. The devil is in the labels: Semantic segmentation from sentences. *arXiv preprint arXiv:2202.02002*, 2022.

- [19] Jiarui Xu, Shalini De Mello, Sifei Liu, Wonmin Byeon, Thomas Breuel, Jan Kautz, and Xiaolong Wang. Groupvit: Semantic segmentation emerges from text supervision. *arXiv preprint arXiv:2202.11094*, 2022.
- [20] Yunxiang Li, Shuai Wang, Jun Wang, Guodong Zeng, Wenjun Liu, Qianni Zhang, Qun Jin, and Yaqi Wang. Gt u-net: A u-net like group transformer network for tooth root segmentation. In *International Workshop on Machine Learning in Medical Imaging*, pages 386–395. Springer, 2021.
- [21] Riddhish Bhalodia, Ali Hatamizadeh, Leo Tam, Ziyue Xu, Xiaosong Wang, Evrim Turkbey, and Daguang Xu. Improving pneumonia localization via cross-attention on medical images and reports. In *International Conference on Medical Image Computing and Computer-Assisted Intervention*, pages 571–581. Springer, 2021.
- [22] Philip Müller, Georgios Kaassis, Congyu Zou, and Daniel Rückert. Joint learning of localized representations from medical images and reports. *arXiv preprint arXiv:2112.02889*, 2021.
- [23] Jacob Devlin, Ming-Wei Chang, Kenton Lee, and Kristina Toutanova. Bert: Pre-training of deep bidirectional transformers for language understanding. *arXiv preprint arXiv:1810.04805*, 2018.
- [24] Alexey Dosovitskiy, Lucas Beyer, Alexander Kolesnikov, Dirk Weissenborn, Xiaohua Zhai, Thomas Unterthiner, Mostafa Dehghani, Matthias Minderer, Georg Heigold, Sylvain Gelly, et al. An image is worth 16x16 words: Transformers for image recognition at scale. *arXiv preprint arXiv:2010.11929*, 2020.
- [25] Sanghyun Woo, Jongchan Park, Joon-Young Lee, and In So Kweon. Cbam: Convolutional block attention module. In *Proceedings of the European conference on computer vision (ECCV)*, pages 3–19, 2018.
- [26] Ozan Oktay, Jo Schlemper, Loic Le Folgoc, Matthew Lee, Matthias Heinrich, Kazunari Misawa, Kensaku Mori, Steven McDonagh, Nils Y Hammerla, Bernhard Kainz, et al. Attention u-net: Learning where to look for the pancreas. *arXiv preprint arXiv:1804.03999*, 2018.
- [27] Fabian Isensee, Paul F Jaeger, Simon AA Kohl, Jens Petersen, and Klaus H Maier-Hein. nnu-net: a self-configuring method for deep learning-based biomedical image segmentation. *Nature methods*, 18(2):203–211, 2021.
- [28] Jeya Maria Jose Valanarasu, Poojan Oza, Ilker Hacihaliloglu, and Vishal M Patel. Medical transformer: Gated axial-attention for medical image segmentation. In *International Conference on Medical Image Computing and Computer-Assisted Intervention*, pages 36–46. Springer, 2021.
- [29] Jieneng Chen, Yongyi Lu, Qihang Yu, Xiangde Luo, Ehsan Adeli, Yan Wang, Le Lu, Alan L Yuille, and Yuyin Zhou. Transunet: Transformers

make strong encoders for medical image segmentation. *arXiv preprint arXiv:2102.04306*, 2021.

- [30] Hu Cao, Yueyue Wang, Joy Chen, Dongsheng Jiang, Xiaopeng Zhang, Qi Tian, and Manning Wang. Swin-unet: Unet-like pure transformer for medical image segmentation. *arXiv preprint arXiv:2105.05537*, 2021.
- [31] Haonan Wang, Peng Cao, Jiaqi Wang, and Osmar R Zaiane. Uctransnet: Rethinking the skip connections in u-net from a channel-wise perspective with transformer. *arXiv preprint arXiv:2109.04335*, 2021.
- [32] Ramprasaath R Selvaraju, Michael Cogswell, Abhishek Das, Ramakrishna Vedantam, Devi Parikh, and Dhruv Batra. Grad-cam: Visual explanations from deep networks via gradient-based localization. In *Proceedings of the IEEE international conference on computer vision*, pages 618–626, 2017.

Appendix

This appendix contains additional details of Section 3, 4 and a discussion about CNN-Transformer hybrid structure superiority.

A The proof of CNN-Transformer structure superiority

Unlike the previous Vision-and-Language work, our proposed LViT model is innovative in processing images and text. We do not use text encoder and creatively use the interaction between CNN and Vit to extract features.

Proof: For the sake of description, we assume that the patch size in ViT is equal to the kernel size in CNN, which is S . The input image matrix is M , and the output after convolution is Y_{cnn} .

$$Y_{cnn,k}(i, j) = \sum_{\xi=0}^S \sum_{\eta=0}^S f_k(\xi, \eta) * M(i - \xi, j - \eta) \quad (18)$$

$$Y_{cnn}(i, j) = [Y_{cnn,1}(i, j); Y_{cnn,2}(i, j); \dots; Y_{cnn,C}(i, j)] \quad (19)$$

where f_k represents the convolution kernel of the k -th channel, and $Y_{cnn,k}(i, j)$ represents the output of the k -th channel after convolution. The total convolution outputs of C channels form $Y_{cnn}(i, j)$. And the convolution operation $f(x)$ is satisfying shift invariance and scale invariance, i.e., if $Y(x) = f(x) * M(x)$, then we have $Y(x - \delta) = f(x) * M(x - \delta)$ and if $Y(x) = f(x) * M(x)$, then we have $|\delta|Y(x/\delta) = f(x/\delta) * M(x/\delta)$. We can assume that CNN has a certain degree of affine invariance and will learn the shallow features better. Moreover, since the convolutional kernel size is fixed, each can only learn and perceive one aspect of the shallow features from the local information, such as points, lines, and boundary. And since the convolutional kernel $f_k(\xi, \eta)$ of each channel shares the weights on the whole image, convolving the whole image with convolutional kernels that focus on boundary features is equivalent to doing whole-image filtering on the image, which will filter out the boundary. From the above, it is clear that CNN has better extraction ability for local shallow features. Similarly, we set the output of matrix M after multi-head self-attention to be Y_{vit} , as shown in the Eqn. 20, 21, 22, 23 and 24,

$$Q_h = W_h^Q \cdot \text{PatchEmbedding}(M) \quad (20)$$

$$K_h = W_h^K \cdot \text{PatchEmbedding}(M) \quad (21)$$

$$V_h = W_h^V \cdot \text{PatchEmbedding}(M) \quad (22)$$

$$Y_{vit,h} = \text{Softmax} \left(\frac{Q_h^T \cdot K_h}{\sqrt{d}} \right) \cdot V_h \quad (23)$$

$$Y_{vit} = LN ([Y_{vit,1}; Y_{vit,2}; \dots; Y_{vit,H}]) \quad (24)$$

where PatchEmbedding represents the embedding layer used to transform M into a sequence vector. $Y_{vit,h}$ denotes the output of the h -th self-attention head, and d prevent the feature gradient from vanishing after Softmax. LN represents the linear layer, which aims to reduce the dimensionality of the output features. And Q_h , K_h , and V_h in the self-attention mechanism are transformations for their own inputs, $\text{Softmax}\left(\frac{Q_h^T \cdot K_h}{\sqrt{d}}\right) \cdot V_h$ is computing the similarity between them. So the self-attention is essentially focusing on the invariance of the input features. The input features M are the whole image for ViT, so ViT is easier to learn the global features than CNN and more robustness.

B Comparison between natural image and medical image

Compared with natural images, medical images typically have the following characteristics:

1. The positions of human organ in medical images are relatively fixed, whereas the relative positions of different segmented objects in natural images often differ significantly.
2. Boundaries between different regions in medical images are often blurred. And the small gray-scale value differences in the vicinity of the boundaries makes it difficult to extract highly accurate segmentation boundaries. In contrast, for an image taken with an ordinary digital camera, there are often significant color differences for different objects.
3. Medical images are usually obtained with specialized equipment. Medical images are taken with different types of equipment and at different environments, which inevitably leading to distribution shifts. In addition, medical images are difficult to share across institutions due to relevant regulations.

C CNN-ViT Interaction Module

Figure. 7 shows the specific structure of CNN-ViT Interaction Module. Among them, we use the interaction module to help recover the size of ViT feature to be consistent with CNN feature.

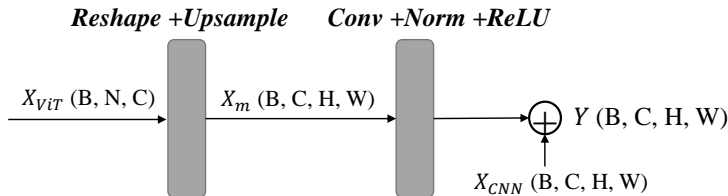


Figure 7: CNN-ViT Interaction Module.

D Details of LV (Language-Vision) Loss

To further utilize the text information to guide the pseudo-label generation, we designed the LV (Language-Vision) loss function. For QaTa-COV19 dataset, we can use different structured text information to form the corresponding mask (the contrastive label). For MoNuSeg dataset, we directly use the mask in labeled training set as the contrastive label. And we calculate the cosine similarity between the texts, as shown in Eqn. 25,

$$\text{TextSim} = \frac{x_{text,p} \cdot x_{text,c}}{|x_{text,p}| \times |x_{text,c}|} \quad (25)$$

where $x_{text,p}$ represents the text feature vector corresponding to the pseudo label, and $x_{text,c}$ represents the text feature vector corresponding to the contrastive label. After that, according to TextSim , we select the contrastive text with the highest similarity and find the segmentation mask corresponding to that text; we calculate the cosine similarity between the predicted segmentation pseudo-label and the contrastive label using the label similarity, as shown in Eqn. 26 and 27,

$$\text{ImgSim} = \frac{x_{img,p} \cdot x_{img,c}}{|x_{img,p}| \times |x_{img,c}|} \quad (26)$$

$$L_{LV} = 1 - \text{ImgSim} \quad (27)$$

where $x_{img,p}$ represents the pseudo-label feature vector, and $x_{img,c}$ represents the comparison label feature vector. Compared to Euclidean distance, cosine similarity is not sensitive to absolute values and reflects the degree of similarity more qualitatively, consistent with our task motivation. The contrastive labels mainly provide labeling information of the approximate location instead of refinement for the boundaries. Therefore, the primary purpose of LV loss is to avoid mis-segmentation or mislabelled cases with significant differences. For this reason, we only use LV loss in the unlabeled case because the contrastive labels are of little help for performance improvement when the data is labeled. And in case of no label, LV loss can avoid the sharp deterioration of the pseudo-label quality.

E Implementation Details

Our proposed approach is implemented using Pytorch. The main parameters of the server are listed below: the operating system is Ubuntu 16.04.12 LTS, the CPU is Intel(R) Xeon(R) Gold 5218, the GPU is a 2-card TESLA V100 32G, and the memory capacity is 128 GB. In addition, for both datasets, we split the train set and the validation set uniformly in the ratio of 80% and 20% from the original train set. Then, the train set is divided into labeled and unlabeled train sets in a specific ratio. The number of samples in the specific dataset is shown in Table 1.

The initial learning rate is set to 3e-4 for the QaTa-COV19 dataset and 1e-3 for the MoNuSeg dataset. We also use an early stop mechanism until the performance of model does not improve for 50 epochs. Different batch sizes are

Table 4: The specific division of datasets.

| | QaTa-COV19 | MoNuSeg |
|-----------|-------------------|----------------|
| Train set | 5716 | 24 |
| Val set | 1429 | 6 |
| Test set | 2113 | 14 |

also set for each dataset since they have different data size. The default batch size is 24 for the QaTa-COV19 dataset, and the default batch size is 4 for the MoNuSeg dataset.

F Loss Function

We set a weighted loss function using the dice loss and cross-entropy loss to form the final loss function. We also add the loss L_{LV} with $\alpha = 0.1$ for the unlabeled data, which are described in the Eqn. 28, 29, 30 and 31,

$$L_{Dice} = 1 - \sum_{i=1}^N \sum_{j=1}^C \frac{1}{NC} \cdot \frac{2|p_{ij} \cap y_{ij}|}{(|p_{ij}| + |y_{ij}|)} \quad (28)$$

$$L_{CE} = - \sum_{i=1}^N \sum_{j=1}^C \frac{1}{N} \cdot y_{ij} \log(p_{ij}) \quad (29)$$

$$L_{sup} = (L_{Dice} + L_{CE})/2 \quad (30)$$

$$L_{unsup} = (L_{Dice} + L_{CE})/2 + \alpha \cdot L_{LV} \quad (31)$$

where N represents the number of pixels, C represents the number of categories, which is set to 2 in our paper. p_{ij} represents the prediction probability that pixel i belongs to category j , y_{ij} represents whether pixel i belongs to category j . If pixel i belongs to category j , then y_{ij} takes 1, otherwise 0.

G Evaluation Metric

For the evaluation metrics, the Dice score and the mIoU metric are used to evaluate the performance of our LViT model and other SOTA methods, as shown in the Eqn. 32 and 33,

$$Dice = \sum_{i=1}^N \sum_{j=1}^C \frac{1}{NC} \cdot \frac{2|p_{ij} \cap y_{ij}|}{(|p_{ij}| + |y_{ij}|)} = 1 - L_{Dice} \quad (32)$$

$$mIoU = \sum_{i=1}^N \sum_{j=1}^C \frac{1}{NC} \cdot \frac{|p_{ij} \cap y_{ij}|}{|p_{ij} \cup y_{ij}|} \quad (33)$$

where N, C, p_{ij} and y_{ij} has the same definition as in the section F.

H Details of the datasets

QaTa-COV19 dataset. Researchers at Qatar University et al. presented the QaTa-COV19 dataset, which consists of 9258 COVID-19 breast radiographs

and their corresponding true segmentation masks. In this dataset, a train set and a test set are artificially split, with the train set consisting of 7145 lung radiographs and the test set consisting of 2113 lung radiographs. And we extend text annotations on the QaTa-COV19 dataset for the first time, with text annotations focusing on whether both lungs are infected, the number of lesion regions, and the approximate location of the infected areas. For example, "Bilateral pulmonary infection, two infected areas, upper left lung and upper right lung." refers to bilateral lung infection, and there are two infection areas located in the upper left lung and the upper right lung respectively. "**Unilateral pulmonary infection, one infected area, middle lower left lung.**" refers to the presence of unilateral pulmonary infection with only one infected area in the middle upper left lung. "**Bilateral pulmonary infection, three infected areas, upper lower left lung and lower right lung.**" refers to bilateral pulmonary infection with three infected areas in the lung, and the three infected areas are in the upper lower left lungs and in the lower right lung. It is important to note that the terms left and right are used from the perspective of the viewer. As can be seen, the above text is similar to a structured annotation that can be easily extracted from the patient's pathology report, and we believe that structured text annotations can provide approximate location of lesion region, which is beneficial for improving segmentation performance.

MoNuSeg dataset. Automatic cell nuclear segmentation techniques can reduce the time required to develop and validate visual biomarkers in pathology analysis. To this end, the MoNuSeg dataset was presented at the MoNuSeg 2018 Challenge, which aims to develop scalable nucleus segmentation techniques in digital pathology and involved 32 teams with more than 80 researchers from different regional institutions. The train set consisted of 30 images with 21,623 single nucleus annotations, and the test set consisted of 14 images. The images in this dataset are from multiple hospitals in The Cancer Genome Atlas (TCGA) and include nuclei from H&E-stained tissue images acquired at the standard 40X magnification. In this work, we introduce text annotations to the MoNuSeg dataset, where the text annotations mainly contain information about the density of the nuclei, e.g., "**The nuclei are sparsely distributed.**" refers to the sparse distribution of nuclei in the image. "**The nuclei are evenly distributed.**" refers to the relatively even distribution of nuclei in the image. All of the above text are manually annotated by viewing the images.

I Ablation study of supervised components on MoNuSeg dateset

It can be seen from the experimental results that DownViT, UpViT, PLAM, and text have certain effects. By introducing DownViT and UpViT modules, dice scores increased by 3.99% and Miou by 5.34% compared with u-net. By introducing the PLAM module, the dice score of LVIT increased by 0.22%, and Miou increased by 0.3%. By introducing text information, the dice score

of LViT also increased by 0.35%, and Miou increased by 0.49%. To further compare the importance of convolution, we also conducted ablation experiments. It can be seen that without convolution, the performance of LViT decreases significantly, the dice score decreases by 2.17%, and Miou decreases by 2.83%. We can also find that by introducing text information, Vit structure can have better performance than CNN. We think it is necessary to use CNN-Transformer as the image encoder.

Table 5: Ablation study on effectiveness of supervised components: DownViT, UpViT, PLAM, Text.

| Method | CNN | DownViT | UpViT | PLAM | Text | Dice (%) | mIoU (%) |
|--------|-----|---------|-------|------|------|--------------|--------------|
| U-Net | ✓ | | | | | 76.45 | 62.86 |
| | ✓ | ✓ | | | | 80.27 | 67.22 |
| | ✓ | ✓ | ✓ | | | 80.44 | 67.41 |
| LViT-L | ✓ | ✓ | ✓ | ✓ | | 80.66 | 67.71 |
| | | ✓ | ✓ | ✓ | ✓ | 78.84 | 65.37 |
| | ✓ | ✓ | ✓ | ✓ | ✓ | 81.01 | 68.20 |

J More qualitative results on QaTa-COV19 and MoNuSeg datasets

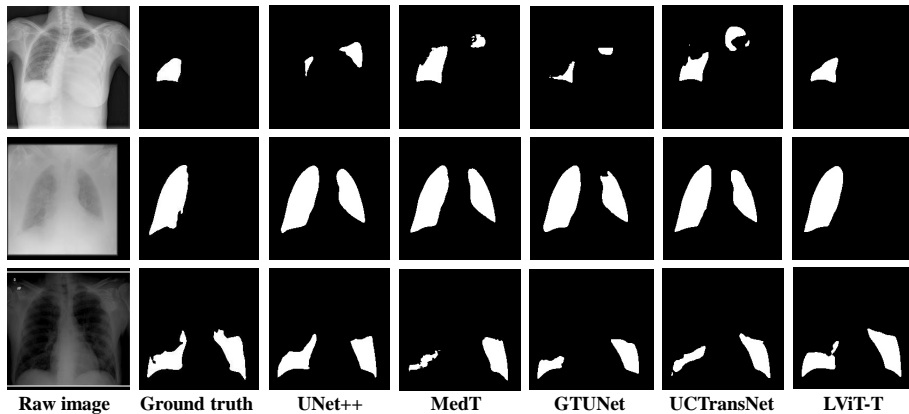


Figure 8: More qualitative results on QaTa-COV19 dataset.

K More saliency maps for interpretability study

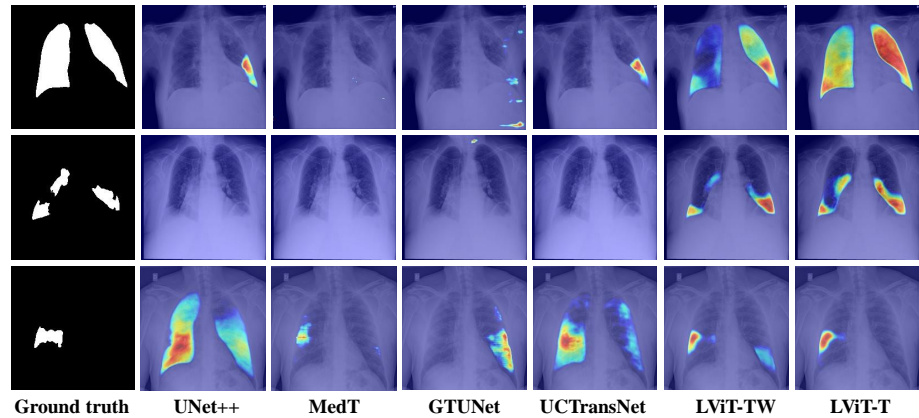


Figure 9: Saliency map for interpretability study of different approaches on QaTa-COV19 dataset.

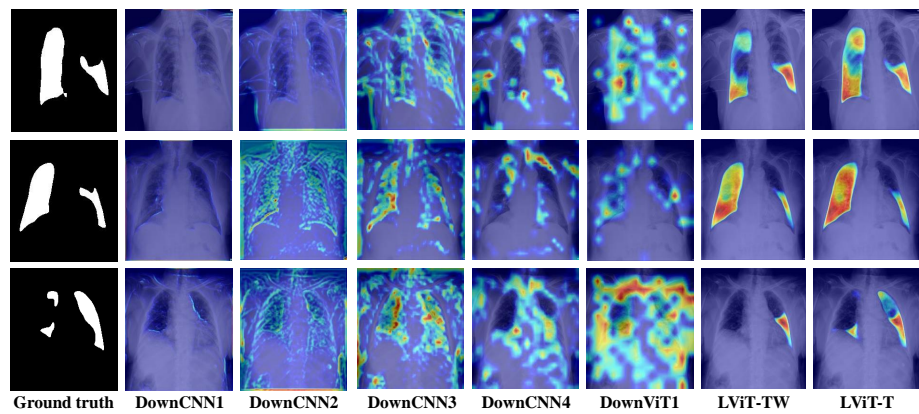


Figure 10: Saliency map for interpretability study of different layers on QaTa-COV19 dataset.